One-Pot Synthesis of W₂C/WS₂ Hybrid Nanostructures for Improved Hydrogen Evolution Reactions and Supercapacitors

Sajjad Hussain [1,2] , **Iqra Rabani** [2], **Dhanasekaran Vikraman** [3] , **Asad Feroze** [4],
Muhammad Ali [5] , **Young-Soo Seo** [2], **Hyun-Seok Kim** [3] , **Seung-Hyun Chun** [4]
and Jongwan Jung [1,2,*]

[1] Hybrid Materials Center (HMC), Sejong University, Seoul 05006, Korea; shussainawan@gmail.com
[2] Department of Nano and Advanced Materials Engineering, Sejong University, Seoul 05006, Korea;
   iqra.rabani@yahoo.com (I.R.); ysseo@sejong.ac.kr (Y.-S.S.)
[3] Division of Electronics and Electrical Engineering, Dongguk University-Seoul, Seoul 04620, Korea;
   v.j.dhanasekaran@gmail.com (D.V.); hyunseokk@dongguk.edu (H.-S.K.)
[4] Department of Physics, Sejong University, Seoul 05006, Korea; asadferoze55@gmail.com (A.F.);
   schun@sejong.ac.kr (S.-H.C.)
[5] Center of Research Excellence in Nanotechnology (CENT), King Fahd University of Petroleum and
   Minerals (KFUPM), Dhahran 31261, Saudi Arabia; muhammadaliaskari@gmail.com
*   Correspondence: jwjung@sejong.ac.kr; Tel.: +82-2-3408-3688; Fax: +82-2-3408-4342

check for updates

Abstract: Tungsten sulfide (WS_2) and tungsten carbide (W_2C) are materialized as the auspicious candidates for various electrochemical applications, owing to their plentiful active edge sites and better conductivity. In this work, the integration of W_2C and WS_2 was performed by using a simple chemical reaction to form W_2C/WS_2 hybrid as a proficient electrode for hydrogen evolution and supercapacitors. For the first time, a W_2C/WS_2 hybrid was engaged as a supercapacitor electrode and explored an incredible specific capacitance of ~1018 F g^{-1} at 1 A g^{-1} with the outstanding robustness. Furthermore, the constructed symmetric supercapacitor using W_2C/WS_2 possessed an energy density of 45.5 Wh kg^{-1} at 0.5 kW kg^{-1} power density. For hydrogen evolution, the W_2C/WS_2 hybrid produced the low overpotentials of 133 and 105 mV at 10 mA cm^{-2} with the small Tafel slopes of 70 and 84 mV dec^{-1} in acidic and alkaline media, respectively, proving their outstanding interfaced electrocatalytic characteristics. The engineered W_2C/WS_2-based electrode offered the high-performance for electrochemical energy applications.

Keywords: hybrid; HER; WS_2; W_2C; symmetric; supercapacitors

1. Introduction

To overcome the ever-increasing energy necessities, researchers have devoted considerable attention to designing and developing new and eco-friendly materials for electrochemical energy production and storage uses [1,2]. Among the various electrochemical storage devices, supercapacitors (SCs) are highly favored, owing to their quick charge–discharge ability, great power density, robust cycling constancy, and simple configuration [3]. SCs are mainly divided into pseudocapacitive and electrical double-layer capacitive (EDLC) behaviors. In the EDLC, energy is filled by the accretion of ions at the junction of electrode/electrolyte. In pseudocapacitors, storage operation is ensued by rapid revocable Faradaic operation between the electro-active species of electrolyte and electrode [3–5]. The commonly used electrode materials for EDLCs have some limitations because of low conductivity or low specific capacitance. The improved capacitance and energy density are to be attained from

pseudocapacitive property, owing to the rapid Faradic reaction. On the other hand, one of the water electrolysis processes of hydrogen evolution reaction (HER) is a prominently accomplished route for green energy. The efficient HER electrocatalysts are improve the rate of electrolysis and produce low overpotential, to reach a specific current density [6,7]. Precious platinum (Pt) is a highly proficient HER electrocatalyst, but costliness and low stability obstruct its commercial use [8,9]. Due to the economic issue, researchers are keen on developing inexpensive and earth-abundant electrode materials [3,10,11].

Transition metal dichalcogenides (TMD) materials, especially metal sulfides (MS_2, M = W, Mo, Co, etc.) are received greater consideration for energy storage and HER devices because of its many beneficial properties such as covalently bonded S−M−S with feeble van der Waals relations between the each layer, efficient mass transport, high specific area, robust edges, and chemical stability [1,12,13]. Moreover, the layered 2D TMD materials own excessive potential as the SC electrode materials, due to their excellent electronic structure, rapid ion intercalation, and preferred pseudocapacitive behavior. However, the low intrinsic conductivity and inactive basal planes are greatly limited to their widespread use [14,15]. In order to circumvent the electrical conductance limitations and to enhance the structural stability and efficiency, TMDs can be hybridized with other high-conducting materials. Carbonaceous materials (graphene or CNT) and transition metal carbides (TMCs) are suitable partner materials for hybridization. TMCs, such as Mo_2C and W_2C, which are newer than graphene and CNT, could be useful electrodes for supercapacitors and HER [16–18]; however, their performance was not widely appealing. The previous reported hybrid materials are $MoSe_2/Mo_2C$ [9], WS_2/reduced graphene oxide hybrids [14,19], $MoS_2/Ti_3C_2T_x$ hybrid [20], MoS_2/WS_2/graphene heterostructures [21], MoS_2/Mo_2C hybrid nanosheets [22], $WS_{(1-x)}Se_x$ decorated 3D graphene [12], graphene supported lamellar 1T'-$MoTe_2$ [23], and MoS_2/reclaimed carbon fiber [24]. Recently, the W_2C/WS_2 has been used as a potential candidate to perceive the enriched catalytic properties for high hydrogen evolution characteristics [25,26]. Furthermore, Wang et al. [27] fabricated $W_xC@WS_2$ heterostructure via carbonizing WS_2 nanotubes, which produced the overpotential of 146 mV at 10 mA cm^{-2} and Tafel slope of 61 mV dec^{-1}. Chen et al. [28] also claimed the Tafel slope of 59 mV dec^{-1} with overpotential of 75 mV at 10 mA cm^{-2} in alkaline medium for a novel eutectoid-structured WC/W_2C heterostructure. The detailed literatures are suggested to combine the W_2C and WS_2 and thereby to progress the electronic and electrochemical properties of resulted hybrid material.

Hence, in this work, W_2C was chosen as a partner material for the hybridization with WS_2, to form W_2C/WS_2 hybrid. This study focused on a simple one-pot strategy to synthesize W_2C/WS_2 as efficient and durable electrodes for electrochemical HER and SCs. So far, few reports are available for W_2C/WS_2 electrocatalysts for HER [26,27,29]. W_2C/WS_2 hybrid, for the first time, is employed as an SCs electrode in this work for improved storage behavior. W_2C/WS_2 possessed an excellent specific capacitance of ~1018 F g^{-1} at 1 A g^{-1} and high cycling stability with 94% retention. Furthermore, symmetric W_2C/WS_2 supercapacitor owned the high energy density of 45.5 Wh kg^{-1} at a low power density of 0.5 kW kg^{-1}. As HER electrocatalyst, low overpotential of 133 and 105 mV was exhibited in acidic and alkaline media, respectively. Synergetic chemical coupling effects between the conducting W_2C and semiconducting WS_2 are believed to contribute significantly improving the electrochemical properties.

2. Materials and Methods

2.1. Synthesis of WS_2 and W_2C Nanostructures

For WS_2 synthesis, 0.5 g tungsten chloride (WO_3) was dispersed in the 2:1 volume ratio of ethanol and DI water mixture, and then the solution was stirred for 30 min, using a magnetic stirrer. Then, 1 g of thiourea was dissolved in aqueous solution, blended, and placed on a hot plate, at 90 °C, with vigorous stirring for 2 h, and then endorsed, to realize the room temperature. Consequently, the dark solution was segregated out by centrifuge, and sediment was cleansed with deionized (DI) water and ethanol and parched at 100 °C, in oven, overnight. Lastly, the synthesized powder was sulfurized, using CVD tubular furnace using argon (Ar) carrier gas at 600 °C for 120 min.

The reported simple chemical reduction route was employed to produce the W_2C nanoparticles [18]. Briefly, 1 g of commercial W_2C powder was dispersed in the ethanol solution (50 mL), with stirring for 3 h, at room temperature. Subsequently, 25 mL of ammonia liquid was poured in the bath mixture and kept to vigorous stirring at 85 °C for 5 h. Then, resulted sediment, after being cleansed using DI water by centrifuge, was kept in an oven, overnight, at 60 °C. The product powder was kept under the gas mixture of H_2 (80 standard cubic centimeters per minute, sccm), CH_4 50 (sccm), and Ar environment in the tubular furnace at 850 °C for 3 h annealing process. Finally, the W_2C powder was collected after the tube attained room temperature.

2.2. Synthesis of W_2C/WS_2 Hybrids

About 1 g of commercial W_2C powder (Sigma Aldrich, Seoul, Korea; CAS number: 12070-12-1) was dispersed in the ethanol solution (50 mL), with stirring, at room temperature, for 3 h. Then 0.25 g WO_3 (Sigma Aldrich, Seoul, Korea; CAS number: 1314-35-8) was dispersed in ethanol and DI water mixture solution. Then 0.5 g of thiourea (Sigma Aldrich, Seoul, Korea; CAS number: 62-56-6) dissolved aqueous solution was blended with W_2C solution and stirred. After that, 2 mL of hydrazine solution and 30 mL of liquid ammonia were mixed with the one-pot solution and stirred for 5 h at 85 °C. The deposit was parted, cleansed with DI water, and dehydrated in a hot oven, overnight, at 60 °C. The powder was post-annealed in a furnace, at 850 °C, for 3 h, under the CH_4 (50 sccm), H_2 (80 sccm), and Ar atmosphere. Figure 1 shows the illustration for the synthesis of a hierarchically W_2C/WS_2 hybrid nanostructure.
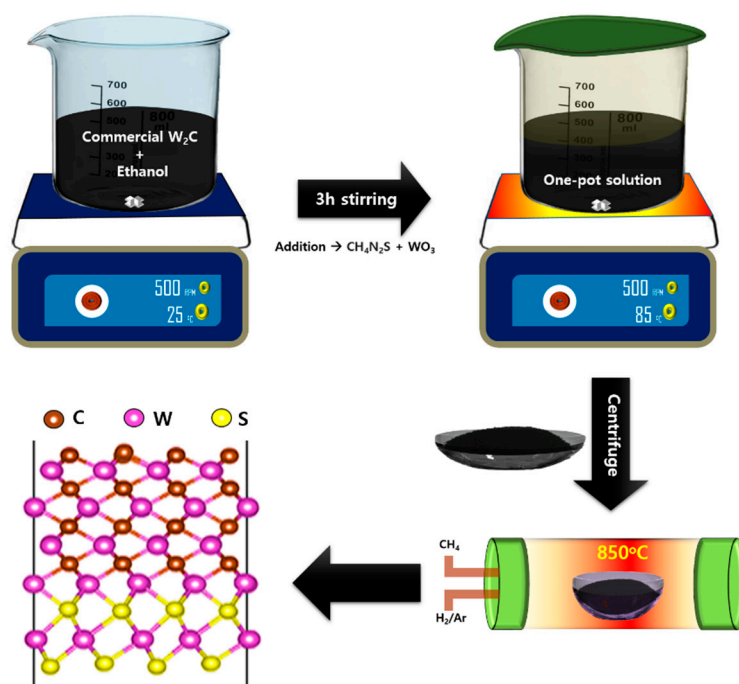

Figure 1. Graphic representation for the synthesis of W_2C/WS_2 hybrid with its derived structure.

2.3. HER Performance

For the working electrode preparation, polyvinylidene fluoride (PVDF), active material (W_2C, WS_2, and W_2C/WS_2), and carbon black at 10:80:10 mass ratio were mixed, and *N*-methyl-2-pyrrolidone (NMP) was added drop-wise. The paste was layered on Ni foam (NF) and overnight dehydrated at 100 °C. For the reference electrode, Ag/AgCl and Hg/HgO were used in acidic and alkaline media performance, respectively, with a graphite counter electrode. We recorded iR corrected linear sweep voltammetry (LSV) by using an electrochemical system (model: 660D; company: CH Instruments, Inc.,

Austin, TX, USA) in 1 M KOH and 0.5 M H_2SO_4 media, with a scan speed of 10 mV s^{-1}. Electrochemical impedance spectroscopy (EIS) results were noted at the frequencies of 0.01 Hz–100 kHz in acid and alkaline media. The HER potential values were converted for reversible hydrogen electrode (RHE) by the following formula: E (vs. RHE) = E (vs. Ag/AgCl) + E^0 (Ag/AgCl) + 0.0592 × pH for acidic medium and E (vs. RHE) = E (vs. Hg/HgO) + E^0 (Hg/HgO) + 0.0592 × pH for alkaline medium.

2.4. Supercapacitor Performance

A biologic science instrument (SP150, Seyssinet-Pariset, France) was used to analyze the supercapacitor properties. The fabrication process for working electrode was same as for HER. The electrochemical performance was employed in 2 M KOH aqueous for three-electrode (denoted as half-cell) and two-electrode (denoted as symmetric) measurements. The active materials (W_2C, WS_2, and W_2C/WS_2) loaded NFs were employed as the working electrodes, along with Ag/AgCl as a reference electrode and a Pt wire as a counter electrode for three electrode measurements. For symmetric, a cut of Whatman filter paper was socked for 2 h in 2 M KOH and then dried, to remove the excess water. As-prepared filter paper was positioned between the couple of similar W_2C/WS_2 electrodes and pressed to make a sandwich structure. Cyclic Voltammetry (CV) and galvanostatic charge–discharge (GCD) scans were noted from −0.8 to + 0.2 V (vs. Ag/AgCl), at different sweep rates and current densities. The capacitance (*C*, F g^{-1}), energy density (*E*, Wh kg^{-1}), and power density (*P*, Wkg^{-1}) were derived by using the Equations (1)–(3), respectively [3,30].

$$C = \frac{(I \times \Delta t)}{(m \times \Delta V)} \tag{1}$$

$$E = \frac{\left(C \times \Delta V^2\right)}{(2 \times 3.6)} \tag{2}$$

$$P = (E \times 3600) / \Delta t \tag{3}$$

where *m* is the mass, *I* is the current, Δt is the discharging time, and ΔV is the potential. EIS studies were accomplished at 10 mV AC amplitude, in an open circuit, in the frequency region of 0.01 Hz to 200 KHz.

2.5. Characterization Details

Field-emission scanning electron microscopy (FESEM) (HITACHI S-4700, Tokyo, Japan) was used to explore the morphological studies. The atomic structures were analyzed by a JEOL-2010F transmission electron microscopy (TEM) with an operation voltage of 200 keV. The Raman spectroscopy (Renishaw inVia RE04, Gloucestershire, UK) measurements were performed in ambient conditions, using the 512 nm Ar laser source with a laser spot size of 1 μm and a scan speed of 30 s. The structural properties were characterized by Rigaku X-ray diffractometer (XRD) (Tokyo, Japan) with Cu-K$_\alpha$ radiation (0.154 nm), at 40 kV and 40 mA, in the scanning range of 10–80° (2θ). For chemical composition and binding energy, the X-ray photoelectron spectroscopy (XPS) measurements were carried out by using an Ulvac PHI X-tool spectrometer (Kanagawa, Japan) with Al K$_\alpha$ X-ray radiation (1486.6 eV). A Brunauer–Emmet–Teller (BET) study to calibrate the surface area of nanostructures was performed, using a N_2 adsorption/desorption medium at 77 K (Micromeritics, Norcross, GA, USA). Pore size distribution was measured with the Barrett–Joyner–Halenda (BJH) analysis.

3. Results and Discussion

3.1. Materials Characteristics

The Raman spectroscopy were performed to measure the crystalline quality and phonon vibration mode properties of W_2C, WS_2, and W_2C/WS_2. Figure 2a displays Raman profiles for W_2C, WS_2, and

W_2C/WS_2. For W_2C, Raman spectrum reveals the solid peaks at 693 and 808 cm^{-1}, which relates to the W–C mode of vibration [31,32]. The sp^2-hybridized graphitic G and defective carbon D related bands observed at 1582 and 1353 cm^{-1}, respectively [32]. For WS_2, the characteristic bands exhibit at 354 and 420 cm^{-1}, which relates to the E_{2g} and A_{1g} mode of vibration, respectively. The additional peaks in the lower frequency regions enabled at 137, 188, and 258 cm^{-1}, referring to J_1, J_2, and A_g mode, support the formation of 1T′ phase WS_2 [33,34]. Interestingly, the synchronized W_2C and WS_2 characteristic peaks appear for W_2C/WS_2 hybrid. The relatively higher intensity for A_{1g} mode than the E_{2g} mode credits to the edge exposed TMD structure, which facilitates the high electrocatalytic activity [35,36].
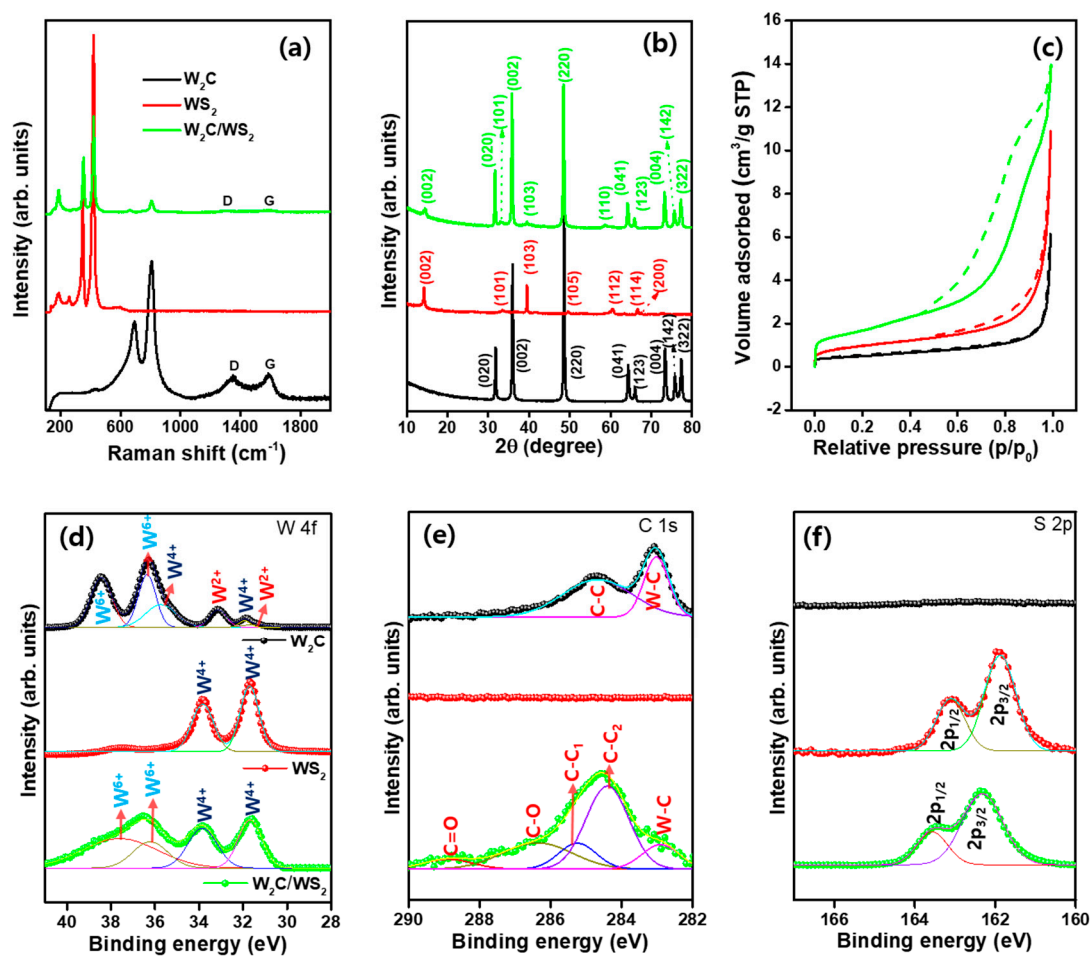

Figure 2. Structural studies of W_2C, WS_2, and W_2C/WS_2. (**a**) Raman profiles, (**b**) X-ray diffraction patterns, (**c**) N_2 sorption isotherms, (**d**–**f**) XPS curves, (**d**) W 4f, (**e**) C 1s, and (**f**) S 2p regions.

The materials structure was validated further by XRD. In Figure 2b, W_2C spectrum shows polycrystalline structure. The (020), (002), (220), (041), (123), (004), (142), and (322) lattice directions observe at 31.5°, 35.1°, 48.8°, 64.1°, 65.8°, 73.2°, 75.6°, and 77.1°, respectively (JCPDS: 89-2371). The diffraction signals at 2θ values of 14.2°, 33.2°, 43.0°, 49.6°, 60.4°, 66.7°, and 67.6° correspond to the (002), (101), (103), (105), (112), (114), and (200) lattices of hexagonal WS_2, respectively (JCPDS: 87-2417). Similar to Raman observation, XRD pattern of W_2C/WS_2 hybrid also produced the cumulative XRD peak positions from W_2C and WS_2 phases, which are indexed with black and red color, respectively. From the structural outcomes, the blended nature of W_2C and WS_2 phase is evidently proved in hybrid with preferential orientation of (220) and (002) lattice planes of W_2C, which might be originated by the dominating behavior of W_2C and their rich presence. Further, the full width at half maximum (FWHM) values were derived from the XRD peaks. The crystallite size was estimated by using FWHM by Scherrer relation [37,38]. The derived FWHM and crystallite values are provided in the Supplementary

Materials Tables S1–S3 for W_2C, WS_2, and W_2C/WS_2, respectively. The estimated mean size (τ) are at 22.9, 18.7, and 18.1 nm for W_2C, WS_2, and W_2C/WS_2, respectively. The reduced-nanosize crystallites for hybrid can be originated by interconnection mechanism between W_2C and WS_2 and their modified crystallographic structure. The d-spacing values were estimated by the Bragg's law ($2d \sin\theta = n\lambda$), and their values are well correlated with the standard results [25]. The extracted values are provided in the Supplementary Materials Tables S1–S3 for W_2C, WS_2, and W_2C/WS_2, respectively. The observed d-spacing values are considerably strained for hybrid compared with pristine, which might be due to the interfacial bonding nature.

The BET surface area was examined to assess the area and pore size distributions by using an N_2 adsorption/desorption medium at 77 K. Figure 2c shows the N_2 isotherms. W_2C/WS_2 possessed a maximum surface area of 6.368 m^2g^{-1}, equated with WS_2 (3.405 m^2g^{-1}) and W_2C (1.75 m^2g^{-1}). The measured total pore volume was 0.009, 0.016, and 0.020 cm^3g^{-1} for W_2C, WS_2, and W_2C/WS_2, respectively (Supplementary Materials Figure S1). The high porosity of W_2C/WS_2, compared with pure, is believed to give the significant contribution of enhancing the electrocatalytic activity by promoting the electrolyte diffusion into the electrode.

XPS was employed to describe the composition and valence states of constructed material. The survey profiles are given in the Supplementary Materials Figure S2, to prove the coexistence of all the elements. The high-resolution XPS profiles for W 4f, C 1s, and S 2p states are provided in Figure 2d–f. From a W 4f XPS profile of W_2C (Figure 2d), the deconvoluted peaks reveal the W^{2+} (31.4 and 33.1 eV), W^{4+} (31.8 and 35.69 eV), and W^{6+} (37.0 and 38.3 eV) doublets. For WS_2, the W4f core level peaks are located at 31.7 and 33.9, due to $W4f_{7/2}$ and $W4f_{5/2}$, respectively. W 4f region of W_2C/WS_2 reveals the peaks at 31.7 eV ($W4f_{7/2}$) and 33.8 eV ($W4f_{5/2}$) with the W^{6+} couplets (37.6 and 36.2 eV) [39,40]. Figure 2e shows the C 1s profile and explores the graphitic sp^2 carbon peak at 284.7 eV and W-C peak at 283.0 eV for W_2C [6]. For the W_2C/WS_2 hybrid, C 1s spectrum produced the $C-C_1$ (284.4 eV), $C-C_2$ (285.2 eV), W-C (282.9 eV), C-O (286.3 eV), and C=O (288.9 eV) peaks [29,41,42]. Figure 2f deconvolution peaks reveal the S 2p couplets of $S2p_{1/2}$ and $S2p_{3/2}$ at 163.1 and 161.8 eV for WS_2, whereas, they are at 163.6 and 162.3 eV for the W_2C/WS_2 hybrid, respectively [43,44]. The atomic percentage of W_2C/WS_2 hybrid is determined to be 32.13%, 22.20%, and 45.67% for W, C, and S atoms, respectively, which is well correlated with EDX results (discussed later). The observed elemental confirmation proved the formation of W_2C/WS_2 hybrid.

Surface characteristics were further elaborated by FESEM and TEM examinations. Figure 3 shows the FESEM micrographs of W_2C, WS_2, and W_2C/WS_2. FESEM micrographs clearly picture the formation of different sizes of nanograins by chemical reduction process in the W_2C nanoparticles (Figure 3a). Nano-spherical-shaped agglomerated grains exhibit for WS_2 (Figure 3b). The sizes of the grains are considerably varied in the nanoscales, due to the bulk agglomeration process during the annealing. In the hybrid, the spherically shaped W_2C particles seem to cover the WS_2 particles (Figure 3c) due to the interconnected mechanism. Reduced sizes of the grains appear with cauliflower like agglomerated grain bunches and well-interconnected domain structure for W_2C/WS_2 hybrid. To prove the hybrid formation, EDX spectrum for W_2C/WS_2 clarifies the elemental composition, as shown in Figure 3d. Furthermore, the mapping images are provided to confirm the equal distribution of all the elements in the hybrid (Figure 3e–h).

TEM measurements were carried out for W_2C/WS_2 hybrid (Figure 4). The different magnification TEM images are provided in Figure 4a–c. Vertically aligned nano-stirpes-like structures are broadly exhibited for the hybrid. The interconnection between the layered fringes and finger-printed structures is clearly visualized. Due to the polycrystalline lattices for W_2C/WS_2 hybrid, the different widths of the lattice fringes are obviously demonstrated in the TEM images (Figure 4b,c). A higher magnification TEM image (Figure 4d) explores the layer structure with the cross-section of different lattice fringes in the W_2C/WS_2 hybrid (inset—fast Fourier transform (FFT), left panel). The phase profile spectrum, extracted by point mask mode and inverse FFT (iFFT, right panel) pattern of inset Figure 4d, shows 6.2 nm spacing which related to (002) WS_2 lattice orientation (Figure 4e). The fingerprint structured

grains interface with layered WS_2 (Figure 4f–g) [44]. The phase profile spectrum, extracted from the iFFT pattern of inset Figure 4g, elevates 2.9 nm spacing, which is related to (020) W_2C lattice orientation (Figure 4h).
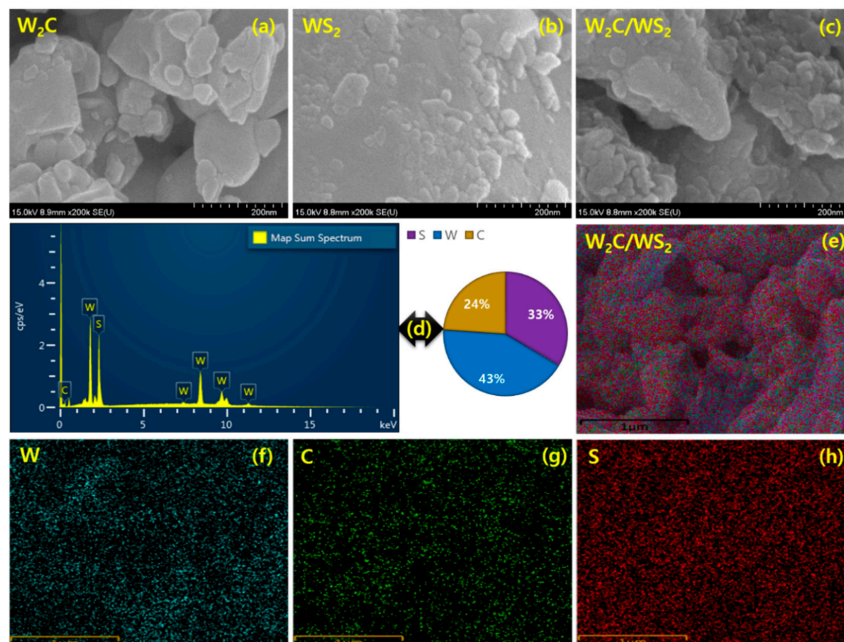

Figure 3. FESEM images of (**a**) W_2C, (**b**) WS_2, and (**c**) W_2C/WS_2 hybrid. (**d**) EDX spectrum of W_2C/WS_2 hybrid; (**e**) mapping image of W_2C/WS_2 hybrid and its elements, (**f**) W, (**g**) C, and (**h**) S.
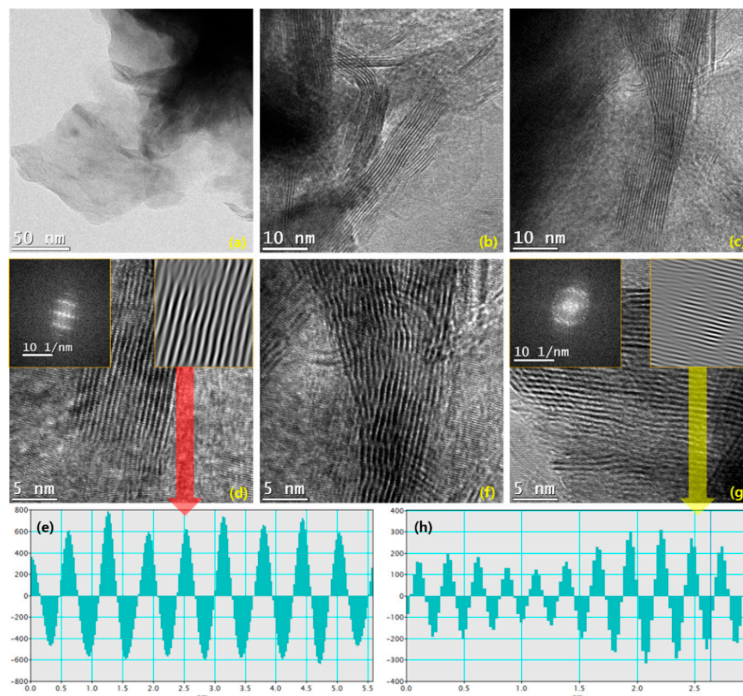

Figure 4. HRTEM images for W_2C/WS_2 hybrid. (**a**) Low- and (**b,c**) high-resolution TEM images. (**d**) Layered WS_2 structure with the inset of FFT and iFFT patterns. (**e**) Phase profile spectrum for (002) lattice orientation of WS_2 with 6.2 nm spacing in the W_2C/WS_2 hybrid. (**f,g**) High-resolution TEM images for W_2C related portion in the hybrid with inset of FFT and iFFT patterns. (**h**) Phase profile spectrum for (020) lattice orientation of W_2C with 2.9 nm spacing in the W_2C/WS_2 hybrid.

3.2. Hydrogen Evolution Studies

Active-materials-coated NFs were engaged as working electrodes to appraise the HER activities in 0.5 M H_2SO_4 and 1 M KOH electrolytes, at room temperature. Figure 5a explores iR-recompensed LSV polarization profiles in 0.5 M H_2SO_4, using 10 mV s^{-1} sweep speed. The W_2C and WS_2 produce 171 and 242 mV to attain 10 mA cm^{-2}, respectively. In contrast, the W_2C/WS_2 hybrid produces an overpotential of 133 mV at 10 mA cm^{-2} (51 mV @ 10 mA cm^{-2} for Pt/C). The exhibited low overpotential credits to interfacial active edges sharing and rapid electron conductivity in the W_2C/WS_2 which proves the importance of hybrid formation. In the 1 M KOH media (Figure 5b), the W_2C/WS_2 electrode also produces highly dynamic HER behavior with a small overpotential of 105 mV at 10 mA cm^{-2} than WS_2 (189 mV) and W_2C (123 mV). The HER performance of W_2C/WS_2 is superior to most of the hybrid-based electrodes (Figure 5c) [45–48]. Li et al. [29] have prepared the nanocomposite of N, S-decorated porous carbon matrix encapsulated WS_2/W_2C ($WS_2/W_2C@NSPC$), which delivered the small overpotential of 126 and 205 mV in 0.5 M H_2SO_4 and 1.0 M KOH, respectively. In addition, Nguyen et al. [26] have reported the 170 mV of onset potential with 55.4 mV dec^{-1} of Tafel slope in 0.5 M H_2SO_4 for $W_2C@WS_2$ nanoflowers synthesized by hydrothermal method.
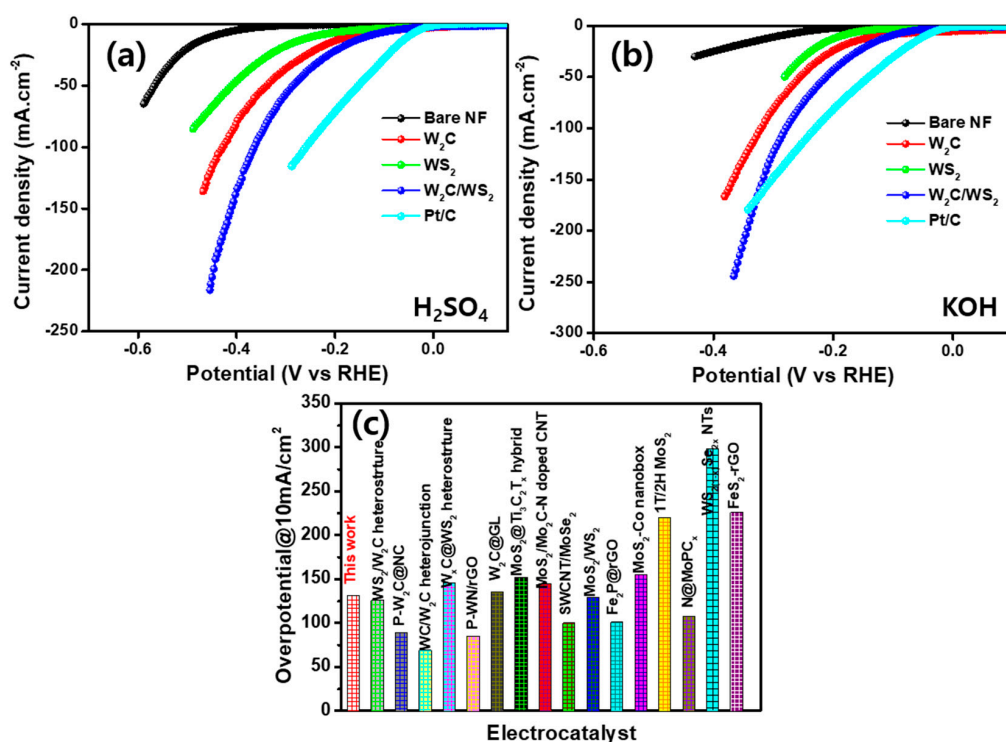

Figure 5. (**a**,**b**) Hydrogen evolution polarization profiles for Pt/C, bare NF, W_2C, WS_2, and W_2C/WS_2 at 10 mV s^{-1} sweep speed in (**a**) 0.5 M H_2SO_4 and (**b**) 1 M KOH media. (**c**) Overpotential comparison of different electrocatalysts.

Tafel slope is a factor to indicate the inherent electrocatalytic activity of the electrode. The Tafel slope values of Pt/C, bare NF, W_2C, WS_2, and W_2C/WS_2 electrocatalysts, are 36, 168, 86, 138, and 70 mV dec^{-1}, respectively, in H_2SO_4 medium (Figure 6a). The outputs prove the outstanding electrocatalytic activity of the W_2C/WS_2 hybrid. Exchange current densities (j_0) assessed by extrapolation Tafel lines to X-axis and their values observe at ~1.03, 1.02, 0.55, and 0.19 mA cm^{-2} for Pt/C, W_2C/WS_2, WS_2, and W_2C, respectively. W_2C, WS_2, and W_2C/WS_2 produce the Tafel slopes of 141, 127, and 84 mV dec^{-1}, respectively, in KOH medium (Figure 6b). The small Tafel slope of W_2C/WS_2 also supports high HER behavior of hybrid electrode in the KOH electrolyte. The extrapolated j_0 is 0.93, 0.72, and 0.38 mA cm^{-2} for W_2C, WS_2, and W_2C/WS_2, respectively, in KOH electrolyte. The exhibited Tafel

slope range suggests that HER involves a Volmer–Heyrovsky mechanism for W_2C/WS_2 hybrid, with electrochemical desorption as the rate-regulatory direction [44,49–51]. Outstanding HER activity in the W_2C/WS_2 hybrid could be explained with electrode kinetics by accumulated electrocatalytic edge facets and a high ratio of charge transfer. The observed HER parameters are provided in Supplementary Materials Table S4 for all the measured electrodes. The j_0 and Tafel values are superior to most reported hybrid electrocatalysts (Figure 6c,d and Supplementary Materials Table S5) [46,48,52]. The low overpotential, large j_0 value, and small Tafel slope in the W_2C/WS_2 hybrid also confirm the importance of hybrid formation for efficient HER electrocatalytic activity in KOH and H_2SO_4 medium.
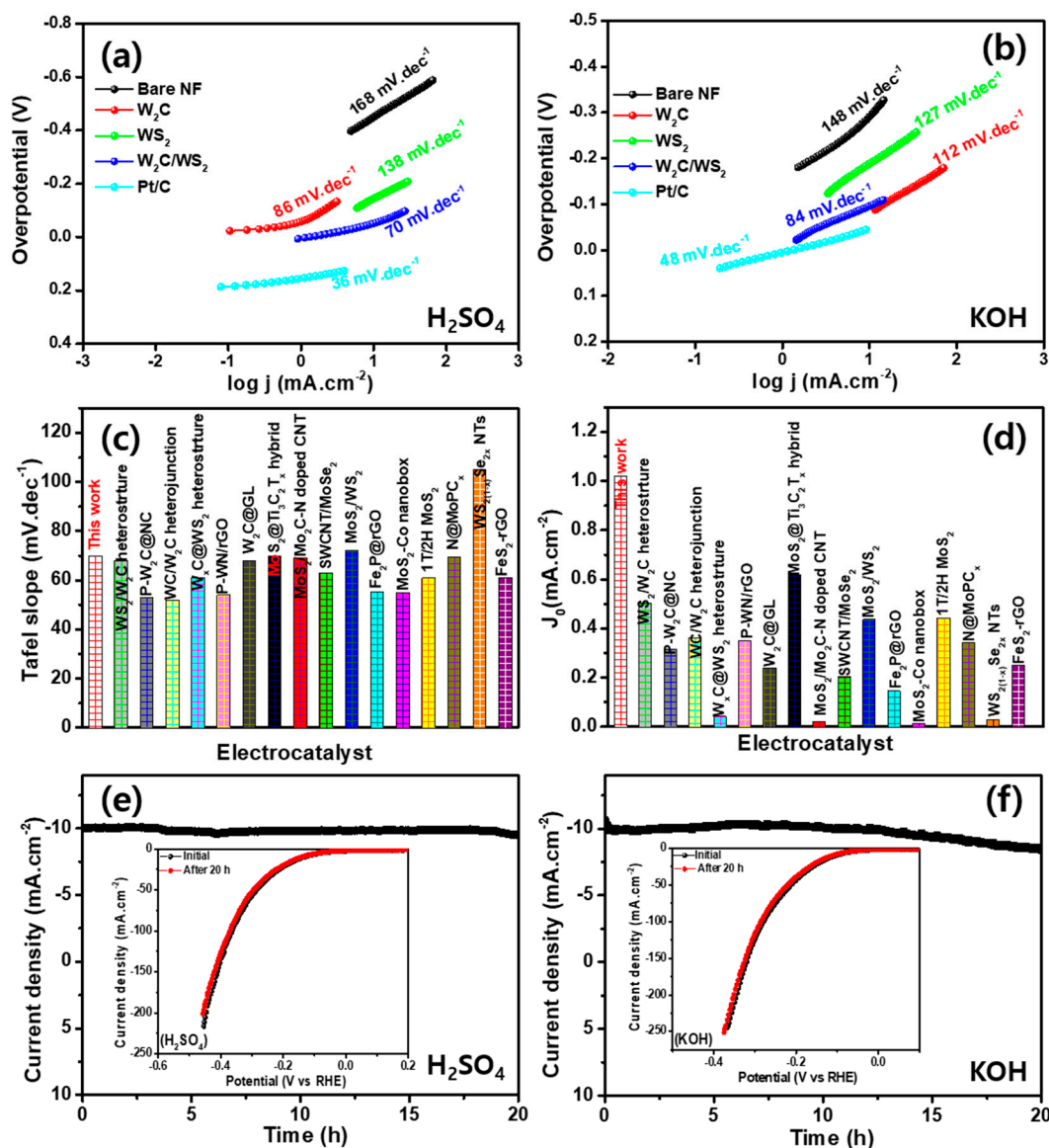

Figure 6. (**a**,**b**) Tafel plots for Pt/C, bare NF, W_2C, WS_2, and W_2C/WS_2 hybrid at 10 mV s^{-1} sweep speed in (**a**) 0.5 M H_2SO_4 and (**b**) 1 M KOH media; comparison of (**c**) Tafel slope and (**d**) exchange current density with different electrocatalysts; chronoamperometric profile of W_2C/WS_2 hybrid for 20 h continuous hydrogen evolution reaction (HER) operation in (**e**) 0.5 M H_2SO_4 and (**f**) 1 M KOH electrolyte (inset: LSV curves before and after 20 h operation).

CV profiles were acquired in the non-Faradaic region, to estimate the double-layer capacitance (C_{dl}) (Supplementary Materials Figure S3a–c). The C_{dl} by linear fitting (Supplementary Materials Figure S3c) are 3.81 mF cm^{-2} (in H_2SO_4) and 3.33 mF cm^{-2} (in KOH) for the W_2C/WS_2 hybrid.

Electrochemical surface areas are 108 and 83 cm^2 in H_2SO_4 and KOH, respectively. A stability and durability evaluation of W_2C/WS_2 electrode was carried out by using chronoamperometric response at a persistent 133 and 105 mV overpotential in H_2SO_4 and KOH (Figure 6e,f), respectively. No significant decline is observed over 20 h in H_2SO_4 the medium, whereas slight deterioration is exhibited for the KOH medium. Note the excellent robustness of W_2C/WS_2 electrode in the H_2SO_4, rather than KOH, medium for HER. LSV curves at initial and after 20 h of continuous HER operation are shown in the inset of Figure 6e,f, respectively.

To probe insights for electrocatalytic activity of materials, EIS was performed in the H_2SO_4 and KOH (Supplementary Materials Figure S4). The observed EIS plot revealed the low charge-transfer resistance (R_{ct}) and swift electron transfer via the electrolyte–electrode interface for W_2C/WS_2. The charge-transfer resistances, R_{ct}, of W_2C/WS_2 (~1.8–2.2 Ω) in the H_2SO_4 and KOH media are lower than those of W_2C and WS_2. Moreover, the small series of resistances (~1.5–2.5 Ω) of all the electrodes suggests that the active materials are well integrated with the porous NF. The high electrocatalytic properties and robust solidity of the W_2C/WS_2 hybrid support it as a potential material to substitute Pt in HER application.

3.3. Supercapacitor Performances

Electrochemical storage properties were elucidated by CV and GCD tests in 2 M KOH electrolyte, using three electrodes, as explained in the experimental part of the manuscript. The CVs were recorded with the potential interval of −0.8 to 0.2 V vs. Ag/AgCl at 10 mV s^{-1} sweep speed for the W_2C, WS_2, and W_2C/WS_2 electrodes (Figure 7a). All the electrodes produce the identical CV loops with Faradaic-adsorptions-blended EDLC operations [53]. The W_2C/WS_2 hybrid electrode shows a wider electrochemical area than the W_2C and WS_2. Moreover, the W_2C/WS_2 hybrid shows a couple of redox peaks (−0.61 and −0.25 V), indicating the reversible reaction from W^{4+} to W^{6+}, corresponding to the proton's absorption/desorption into the WS_2 interlayers [54]. Figure 7b shows CVs of various scan rates (10–50 mV s^{-1}), and their shapes are maintained, indicating good electrochemical capacitive characteristics and high-rate performance. The results for WS_2 and W_2C at various scan speeds are shown in Supplementary Figure S5a,b, respectively. Successive 100 CV cycles were executed in the potential region of −0.8 to 0.2 V, to assess the stability for the W_2C/WS_2 electrode, and its output is presented Figure 7c. Due to the EDLC-combined Faradaic storage mechanism, it possesses good stability with minimal degradation over the repeated cycles [55].

The electrochemical storage performance was further tested by GCD curves, as shown in Figure 8a–d. The slightly distorted triangle like the GCD curve is exhibited for the W_2C/WS_2 and WS_2 electrodes, due to the redox reaction. For the W_2C electrode, a square-structured GCD curve is exhibited, with a voltage drop, due to the easy oxidation characteristic. The W_2C/WS_2 electrode exposes an outstanding specific capacitance (estimated by using the Equation (1)) of 1018 F g^{-1}, as compare to the WS_2 (~158 F g^{-1}) and W_2C (~133 F g^{-1}), at the current density of 1 A g^{-1}. GCD analysis displays similar curves at the different current densities. Observe the specific capacitances of 133, 90, 66, and 50 F g^{-1} for W_2C (Figure 8b) and 158, 120, 87, and 80 F g^{-1} for WS_2 (Figure 8c) at 1, 2, 3, and 5 A g^{-1} current density, respectively. For W_2C/WS_2, a high specific capacitance of 1018, 866, 816, and 660 F g^{-1} exhibits at the 1, 2, 3, and 5 A g^{-1} current density, respectively (Figure 8d). The specific capacitance changes with current density, as shown in Supplementary Materials Figure S6. The significant enhancement of capacitances for W_2C/WS_2 electrode credits to the mutual interactions between W_2C and WS_2, large surface area, rich active edge facets of WS_2, and high electronic conductivity of W_2C to enable the rapid transference of electrons during a charge–discharge process. Supplementary Materials Table S6 provides the extended comparison of W_2C/WS_2 SCs performance with the previously reported hybrid electrodes.
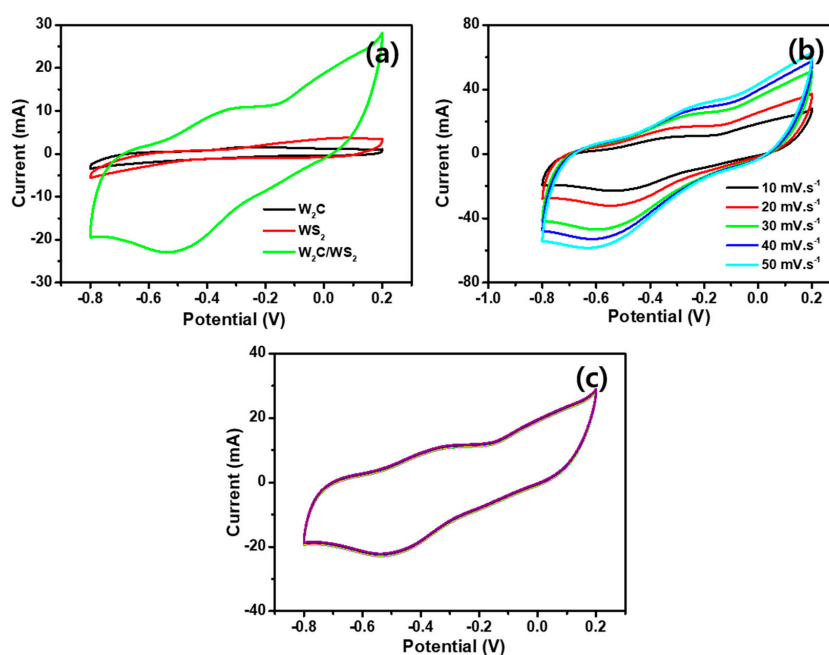
Figure 7. Supercapacitor Cyclic Voltammetry (CV) for three electrode measurement: (**a**) CV curves for W_2C, WS_2, and W_2C/WS_2 electrodes; (**b**) different scan rate CV curves for the W_2C/WS_2 hybrid; (**c**) multiple cycle CV curves for the W_2C/WS_2 hybrid.
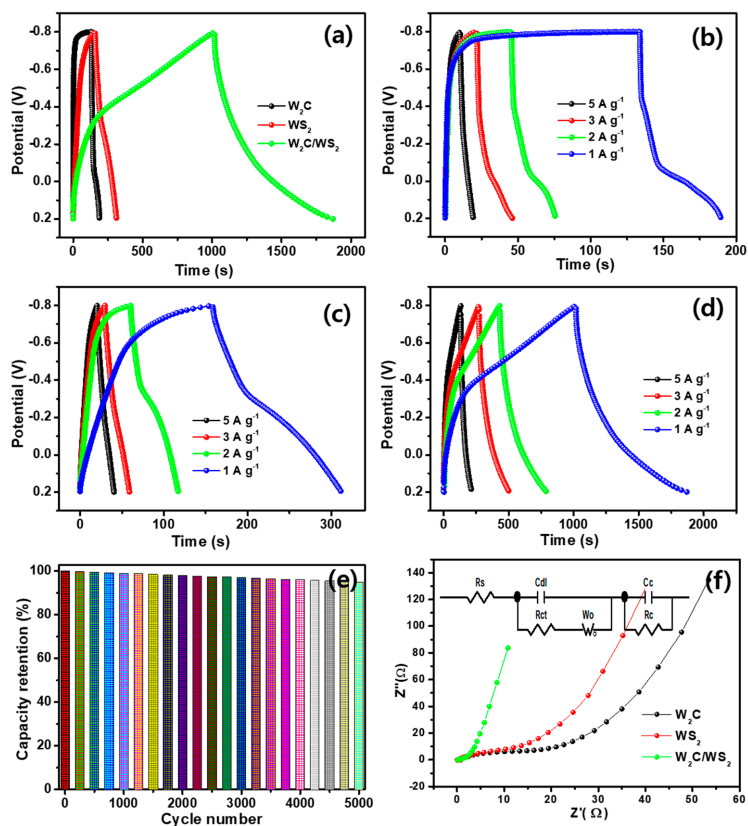

Figure 8. (**a–d**) Galvanostatic charge–discharge (GCD) profiles for three electrode measurement; (**a**) GCDs at 1 Ag^{-1} for W_2C, WS_2, and W_2C/WS_2; GCDs at different current densities for (**b**) W_2C, (**c**) WS_2, and (**d**) W_2C/WS_2; (**e**) stability performance of W_2C/WS_2 hybrid; (**f**) EIS curves for W_2C, WS_2, and W_2C/WS_2 (inset-fitted circuit).

Cyclic stability is an essential property for the supercapacitor electrodes. In the case of the W_2C/WS_2 electrode, 94% of primary capacitance was perceived after 5000 cycles (Figure 8e), suggesting long-term stability. EIS measurements were performed to prove the charge-transfer characteristics (Figure 8f). Fitted curve from the Nyquist profile is inserted in Figure 8f, where C_{dl} is the double-layer capacitance, R_{ct} is the charge-transfer resistance, R_s is the series resistance, W_o the Warburg impedance at open circuit voltage, and R_c and C_c are the capacitive resistance and capacitive capacitance, respectively. The output curve indicates that the charge-transfer resistance significantly reduces for W_2C/WS_2 hybrid electrode, as compared to their pristine. A lower R_{ct} (~1.0 Ω) was obtained by the hybrid electrode, as compared to the WS_2 (~13.9 Ω) and W_2C (10.1 Ω), respectively.

To assess the practical application, the symmetric supercapacitor (SSC) was assembled with two identical W_2C/WS_2 hybrid electrodes. The electrochemical CV measurement of SSC was measured by using the similar potential range of half-cell measurements. Figure 9a shows the CV curves for W_2C/WS_2 symmetric cell device. The modified rectangular shape of CV curve for the W_2C/WS_2 hybrid SSC reveals slightly shouldered redox reaction, confirming the key contribution of EDLC characteristics. The constructed SSC device gives an excellent current response and larger integral area, compared to previous TMDs-based materials [56,57]. The different scan rates, using performed CV curves, prove the high rate of capability of the prepared SSC devices. Figure 9b shows the different current densities, using prepared SSC GCD curves, indicating the excellent electrochemical rate capability. The charge/discharge time considerably decreases for the SSC device due to its direct intercalation and extraction of ions through the solid electrolyte, compared with its half-cell outcomes. The capacitance value of symmetric device was valued from the GCD curve, using Equation (1) [58]. The W_2C/WS_2 hybrid delivers the higher symmetric capacitance of 328, 306, 255, and 220 F g^{-1} at 1, 2, 3, and 5 A g^{-1} of current densities, respectively, as presented in Figure 9c. Interestingly, our symmetric device results show the enhancing capacitance, compared to other symmetric capacitor results [56,59,60]. The specific energy and specific power values are significant for the practical uses, which were weighed by relations 2 and 3, respectively. The symmetric device carries the energy densities of 45.5, 42.5, 35.4, and 30.5 Wh kg^{-1} at 0.5, 1.0, 1.5, and 2.0 kW kg^{-1} power density, respectively, as given in the Figure 9d.
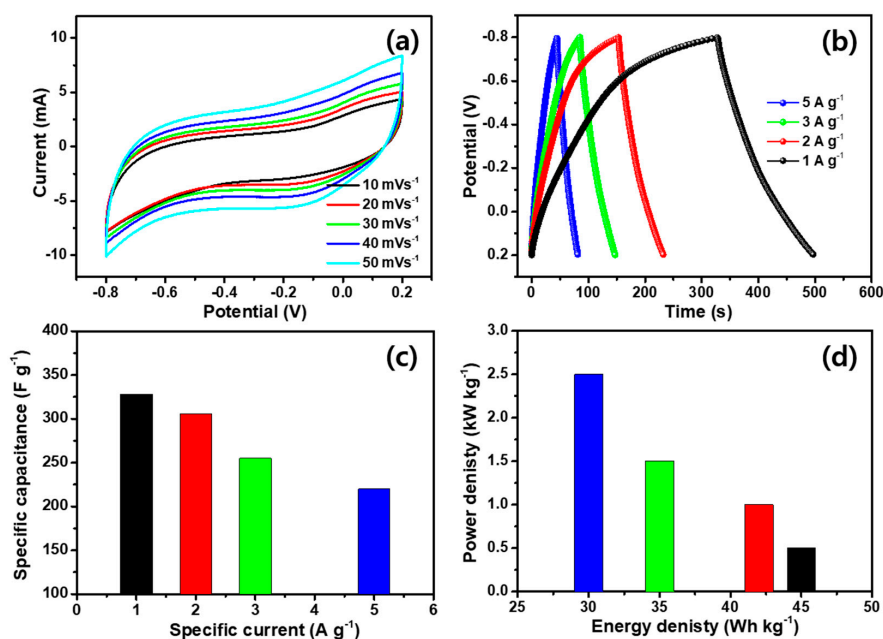

Figure 9. Symmetric supercapacitor performance of W_2C/WS_2. (**a**) Different scan rate CV curves for symmetric W_2C/WS_2 hybrid; (**b**) GCDs for symmetric W_2C/WS_2 at different current densities; (**c**) specific capacitance at various scan rates for W_2C/WS_2 by symmetric measurements; (**d**) Ragone plots of W_2C/WS_2 for symmetric device.

The exhibited energy density of symmetric W_2C/WS_2 capacitor is superior to the recently reported symmetric devices using TMDs and TMCs electrodes, MoS_2 sheets (18.43 Wh kg^{-1}) [60], $Ti_3C_2T_x$/MWCNT (3 Wh kg^{-1}) [61], s-MoS_2/CNS (7.4 Wh kg^{-1}) [62], 3D-graphene/MoS_2 (24.59 Wh kg^{-1}) [63], MoS_2/RCF (22.5 Wh kg^{-1}) [24], MoS_2/RGO/MoS_2@Mo (6.22 Wh kg^{-1}) [56], and MoS_2 sponge (6.15 Wh kg^{-1}) [59]. Overall, our findings demonstrate that the inclusion of carbide-based material with TMDs deliberately improves the conductance of the hybrid material, assists swift conveyance of electrons/ion, and improves the stability of electrode material.

4. Conclusions

We have successfully engineered the W_2C/WS_2 hybrid electrode by a simple cost-effective one-pot chemical reaction. Highly conductive W_2C-supported WS_2 hybrids were designed to promote high electrocatalytic activity for HER and SCs by accumulating the number of active edges and facilitating the swift electron transport. In the case of HER, the interfaced W_2C/WS_2 hybrid produced the small overpotentials of 133 and 105 mV, to achieve the 10 mA cm^{-2} current density with the Tafel slope of 70 and 84 mV dec^{-1} in H_2SO_4 and KOH media, respectively, which proved the outstanding electrocatalytic HER characteristics. Half-cell measurements unveiled the remarkable specific capacitance of ~1018 F g^{-1} at 1 A g^{-1} with the rate competency nature and robust responses for W_2C/WS_2 hybrid electrode. W_2C/WS_2-based symmetric supercapacitor exposed the specific energy of 45.5 Wh kg^{-1} at 0.5 kW kg^{-1} specific power with a capacitance of 328 F g^{-1} at 1 A g^{-1} current density. The suggested low-cost methodology of one-pot reaction is highly feasible to fabricate the efficacious nanostructured hybrids and has larger-scale production capability because of its controlled synthesis process. Hence, the developed hybrid material and methodology have a broad scope for the future electrochemical applications.

Supplementary Materials: The following are available online at http://www.mdpi.com/2079-4991/10/8/1597/s1. Figure S1: Pore diameter versus pore volume variations for the nanostructures. Figure S2: Survey XPS spectrum of (a) W_2C, (b) WS_2, and (c) W_2C/WS_2. Figure S3: CV spectra in the non-Faradaic region with different scan rates for W_2C/WS_2 hybrid HER electrodes in (a) 0.5 M H_2SO_4 and (b) 1 M KOH electrolyte and (c) their current differences. Figure S4: EIS spectra of Pt, W_2C, WS_2, and W_2C/WS_2 hybrids electrodes in (a) 0.5 M H_2SO_4 and (b) 1M KOH electrolyte. Figure S5: CV curves for the (a) WS_2 and (c) W_2C electrodes at various scan rates, using half-cell (10–50 mVs^{-1}). Figure S6: The specific capacitance variations at different current densities for W_2C, WS_2, and W_2C/WS_2 electrodes by half-cell measurements. Table S1: Microstructural parameters of W_2C. Table S2: Microstructural parameters of WS_2. Table S3: Microstructural parameters of W_2C/WS_2. Table S4: Comparison of electrochemical parameters for different electrocatalysts. Table S5: HER catalytic performances TMDs and TMCs-based electrocatalysts. Table S6: Performances of TMDs- and TMCs-based electrodes for supercapacitors.

References

1. Vikraman, D.; Akbar, K.; Hussain, S.; Yoo, G.; Jang, J.-Y.; Chun, S.-H.; Jung, J.; Park, H.J. Direct synthesis of thickness-tunable MoS_2 quantum dot thin layers: Optical, structural and electrical properties and their application to hydrogen evolution. *Nano Energy* **2017**, *35*, 101–114. [CrossRef]

2. Sarma, P.V.; Kayal, A.; Sharma, C.H.; Thalakulam, M.; Mitra, J.; Shaijumon, M. Electrocatalysis on edge-rich spiral WS$_2$ for hydrogen evolution. *ACS Nano* **2019**, *13*, 10448–10455. [CrossRef] [PubMed]

3. Vikraman, D.; Karuppasamy, K.; Hussain, S.; Kathalingam, A.; Sanmugam, A.; Jung, J.; Kim, H.-S. One-pot facile methodology to synthesize MoS$_2$-graphene hybrid nanocomposites for supercapacitors with improved electrochemical capacitance. *Compos. Part. B Eng.* **2019**, *161*, 555–563. [CrossRef]

4. Liu, Y.; Peng, X. Recent advances of supercapacitors based on two-dimensional materials. *Appl. Mater. Today* **2017**, *8*, 104–115. [CrossRef]

5. Wazir, M.B.; Daud, M.; Ullah, N.; Hai, A.; Muhammad, A.; Younas, M.; Rezakazemi, M. Synergistic properties of molybdenum disulfide (MoS$_2$) with electro-active materials for high-performance supercapacitors. *Int. J. Hydrog Energy* **2019**, *44*, 17470–17492. [CrossRef]

6. Zhang, H.; Pan, Q.; Sun, Z.; Cheng, C. Three-dimensional macroporous W$_2$C inverse opal arrays for the efficient hydrogen evolution reaction. *Nanoscale* **2019**, *11*, 11505–11512. [CrossRef]

7. Attanayake, N.H.; Thenuwara, A.C.; Patra, A.; Aulin, Y.V.; Tran, T.M.; Chakraborty, H.; Borguet, E.; Klein, M.L.; Perdew, J.P.; Strongin, D.R. Effect of intercalated metals on the electrocatalytic activity of 1T-MoS$_2$ for the hydrogen evolution reaction. *ACS Energy Lett.* **2017**, *3*, 7–13. [CrossRef]

8. Hussain, S.; Vikraman, D.; Akbar, K.; Naqvi, B.A.; Abbas, S.M.; Kim, H.-S.; Chun, S.-H.; Jung, J. Fabrication of MoSe$_2$ decorated three-dimensional graphene composites structure as a highly stable electrocatalyst for improved hydrogen evolution reaction. *Renew. Energy* **2019**, *143*, 1659–1669. [CrossRef]

9. Vikraman, D.; Hussain, S.; Karuppasamy, K.; Feroze, A.; Kathalingam, A.; Sanmugam, A.; Chun, S.-H.; Jung, J.; Kim, H.-S. Engineering the novel MoSe$_2$-Mo$_2$C hybrid nanoarray electrodes for energy storage and water splitting applications. *Appl. Catal. B Environ.* **2020**, *264*, 118531. [CrossRef]

10. Huang, M.; Li, F.; Dong, F.; Zhang, Y.X.; Zhang, L.L. Mno$_2$-based nanostructures for high-performance supercapacitors. *J. Mater. Chem. A* **2015**, *3*, 21380–21423. [CrossRef]

11. Ramesh, S.; Vikraman, D.; Karuppasamy, K.; Yadav, H.M.; Sivasamy, A.; Kim, H.-S.; Kim, J.-H.; Kim, H.-S. Controlled synthesis of SnO$_2$@NiCo$_2$O$_4$/nitrogen doped multiwalled carbon nanotube hybrids as an active electrode material for supercapacitors. *J. Alloys Compd.* **2019**, *794*, 186–194. [CrossRef]

12. Hussain, S.; Akbar, K.; Vikraman, D.; Afzal, R.A.; Song, W.; An, K.S.; Farooq, A.; Park, J.Y.; Chun, S.H.; Jung, J. Ws$_{(1-x)}$se$_x$ nanoparticles decorated three-dimensional graphene on nickel foam: A robust and highly efficient electrocatalyst for the hydrogen evolution reaction. *Nanomaterials* **2018**, *8*, 929. [CrossRef] [PubMed]

13. Hussain, S.; Chae, J.; Akbar, K.; Vikraman, D.; Truong, L.; Naqvi, A.B.; Abbas, Y.; Kim, H.-S.; Chun, S.-H.; Kim, G.; et al. Fabrication of robust hydrogen evolution reaction electrocatalyst using Ag$_2$Se by vacuum evaporation. *Nanomaterials* **2019**, *9*, 1460. [CrossRef] [PubMed]

14. Tu, C.-C.; Lin, L.-Y.; Xiao, B.-C.; Chen, Y.-S. Highly efficient supercapacitor electrode with two-dimensional tungsten disulfide and reduced graphene oxide hybrid nanosheets. *J. Power Sources* **2016**, *320*, 78–85. [CrossRef]

15. Vikraman, D.; Hussain, S.; Akbar, K.; Karuppasamy, K.; Chun, S.H.; Jung, J.; Kim, H.S. Design of basal plane edges in metal-doped nanostripes-structured MoSe$_2$ atomic layers to enhance hydrogen evolution reaction activity. *ACS Sustain. Chem. Eng.* **2019**, *7*, 458–469. [CrossRef]

16. Esposito, D.V.; Hunt, S.T.; Kimmel, Y.C.; Chen, J.G. A new class of electrocatalysts for hydrogen production from water electrolysis: Metal monolayers supported on low-cost transition metal carbides. *J. Am. Chem. Soc.* **2012**, *134*, 3025–3033. [CrossRef]

17. Hunt, S.T.; Milina, M.; Alba-Rubio, A.C.; Hendon, C.H.; Dumesic, J.A.; Román-Leshkov, Y. Self-assembly of noble metal monolayers on transition metal carbide nanoparticle catalysts. *Science* **2016**, *352*, 974–978. [CrossRef]

18. Hussain, S.; Vikraman, D.; Feroze, A.; Song, W.; An, K.-S.; Kim, H.-S.; Chun, S.-H.; Jung, J. Synthesis of Mo$_2$C and W$_2$C nanoparticle electrocatalysts for the efficient hydrogen evolution reaction in alkali and acid electrolytes. *Front. Chem.* **2019**, *7*, 716. [CrossRef]

19. Ratha, S.; Rout, C.S. Supercapacitor electrodes based on layered tungsten disulfide-reduced graphene oxide hybrids synthesized by a facile hydrothermal method. *ACS Appl. Mater. Interfaces* **2013**, *5*, 11427–11433. [CrossRef]

20. Liu, J.; Liu, Y.; Xu, D.; Zhu, Y.; Peng, W.; Li, Y.; Zhang, F.; Fan, X. Hierarchical "nanoroll" like $MoS_2/Ti_3C_2T_x$ hybrid with high electrocatalytic hydrogen evolution activity. *Appl. Catal. B Environ.* **2019**, *241*, 89–94. [CrossRef]

21. Lin, T.W.; Sadhasivam, T.; Wang, A.Y.; Chen, T.Y.; Lin, J.Y.; Shao, L.D. Ternary composite nanosheets with MoS_2/WS_2/graphene heterostructures as high-performance cathode materials for supercapacitors. *Chem. Electro. Chem.* **2018**, *5*, 1024–1031. [CrossRef]

22. Zhao, Z.; Qin, F.; Kasiraju, S.; Xie, L.; Alam, M.K.; Chen, S.; Wang, D.; Ren, Z.; Wang, Z.; Grabow, L.C. Vertically aligned MoS_2/Mo_2C hybrid nanosheets grown on carbon paper for efficient electrocatalytic hydrogen evolution. *ACS Catal.* **2017**, *7*, 7312–7318. [CrossRef]

23. Liu, M.; Wang, X.; Huang, Z.; Guo, P.; Wang, Z. In-situ solution synthesis of graphene supported lamellar 1T'-$MoTe_2$ for enhanced pseudocapacitors. *Mater. Lett.* **2017**, *206*, 229–232. [CrossRef]

24. Zhao, C.; Zhou, Y.; Ge, Z.; Zhao, C.; Qian, X. Facile construction of MoS_2/RCF electrode for high-performance supercapacitor. *Carbon* **2018**, *127*, 699–706. [CrossRef]

25. Nguyen, T.P.; Choi, K.S.; Kim, S.Y.; Lee, T.H.; Jang, H.W.; Van Le, Q.; Kim, I.T. Strategy for controlling the morphology and work function of W2C/WS_2 nanoflowers. *J. Alloys Compd.* **2020**, *829*, 154582. [CrossRef]

26. Nguyen, T.P.; Kim, S.Y.; Lee, T.H.; Jang, H.W.; Le, Q.V.; Kim, I.T. Facile synthesis of $W_2C@WS_2$ alloy nanoflowers and their hydrogen generation performance. *Appl. Surf. Sci.* **2020**, *504*, 144389. [CrossRef]

27. Wang, F.; He, P.; Li, Y.; Shifa, T.A.; Deng, Y.; Liu, K.; Wang, Q.; Wang, F.; Wen, Y.; Wang, Z. Interface engineered $W_xC@WS_2$ nanostructure for enhanced hydrogen evolution catalysis. *Adv. Funct. Mater.* **2017**, *27*, 1605802. [CrossRef]

28. Chen, Z.; Gong, W.; Cong, S.; Wang, Z.; Song, G.; Pan, T.; Tang, X.; Chen, J.; Lu, W.; Zhao, Z. Eutectoid-structured WC/W_2C heterostructures: A new platform for long-term alkaline hydrogen evolution reaction at low overpotentials. *Nano Energy* **2020**, *68*, 104335. [CrossRef]

29. Li, Y.; Wu, X.; Zhang, H.; Zhang, J. Interface designing over WS_2/W_2C for enhanced hydrogen evolution catalysis. *ACS Appl. Energy Mater.* **2018**, *1*, 3377–3384. [CrossRef]

30. Javed, M.S.; Dai, S.; Wang, M.; Guo, D.; Chen, L.; Wang, X.; Hu, C.; Xi, Y. High performance solid state flexible supercapacitor based on molybdenum sulfide hierarchical nanospheres. *J. Power Sources* **2015**, *285*, 63–69. [CrossRef]

31. Dash, T.; Nayak, B. Preparation of $WC–W_2C$ composites by arc plasma melting and their characterisations. *Ceram. Int.* **2013**, *39*, 3279–3292. [CrossRef]

32. Yan, G.; Wu, C.; Tan, H.; Feng, X.; Yan, L.; Zang, H.; Li, Y. N-carbon coated pw 2 c composite as efficient electrocatalyst for hydrogen evolution reactions over the whole ph range. *J. Mater. Chem. A* **2017**, *5*, 765–772. [CrossRef]

33. Voiry, D.; Yamaguchi, H.; Li, J.; Silva, R.; Alves, D.C.; Fujita, T.; Chen, M.; Asefa, T.; Shenoy, V.B.; Eda, G. Enhanced catalytic activity in strained chemically exfoliated WS_2 nanosheets for hydrogen evolution. *Nat. Mater.* **2013**, *12*, 850–855. [CrossRef] [PubMed]

34. Liu, Z.; Li, N.; Su, C.; Zhao, H.; Xu, L.; Yin, Z.; Li, J.; Du, Y. Colloidal synthesis of 1T'phase dominated WS_2 towards endurable electrocatalysis. *Nano Energy* **2018**, *50*, 176–181. [CrossRef]

35. Gao, M.-R.; Chan, M.K.; Sun, Y. Edge-terminated molybdenum disulfide with a 9.4-Å interlayer spacing for electrochemical hydrogen production. *Nat. Commun.* **2015**, *6*, 1–8. [CrossRef]

36. Wang, H.; Lu, Z.; Kong, D.; Sun, J.; Hymel, T.M.; Cui, Y. Electrochemical tuning of MoS_2 nanoparticles on three-dimensional substrate for efficient hydrogen evolution. *ACS Nano* **2014**, *8*, 4940–4947. [CrossRef]

37. Vikraman, D.; Park, H.J.; Kim, S.I.; Thaiyan, M. Magnetic, structural and optical behavior of cupric oxide layers for solar cells. *J. Alloys Compd.* **2016**, *686*, 616–627. [CrossRef]

38. Sebastian, S.; Kulandaisamy, I.; Valanarasu, S.; Yahia, I.S.; Kim, H.-S.; Vikraman, D. Microstructural and electrical properties evaluation of lead doped tin sulfide thin films. *J. Sol. Gel Sci. Technol.* **2020**, *93*, 52–61. [CrossRef]

39. Gong, Q.; Wang, Y.; Hu, Q.; Zhou, J.; Feng, R.; Duchesne, P.N.; Zhang, P.; Chen, F.; Han, N.; Li, Y. Ultrasmall and phase-pure W_2C nanoparticles for efficient electrocatalytic and photoelectrochemical hydrogen evolution. *Nat. Commun.* **2016**, *7*, 1–8. [CrossRef]

40. Zhang, L.-N.; Ma, Y.-Y.; Lang, Z.-L.; Wang, Y.-H.; Khan, S.U.; Yan, G.; Tan, H.-Q.; Zang, H.-Y.; Li, Y.-G. Ultrafine cable-like WC/W_2C heterojunction nanowires covered by graphitic carbon towards highly efficient electrocatalytic hydrogen evolution. *J. Mater. Chem. A* **2018**, *6*, 15395–15403. [CrossRef]

41. Lewin, E.; Persson, P.Å.; Lattemann, M.; Stüber, M.; Gorgoi, M.; Sandell, A.; Ziebert, C.; Schäfers, F.; Braun, W.; Halbritter, J. On the origin of a third spectral component of C1s XPS-spectra for nc-TiC/a-C nanocomposite thin films. *Surf. Coat. Technol.* **2008**, *202*, 3563–3570. [CrossRef]

42. Li, J.; Zhou, C.; Mu, J.; Yang, E.-C.; Zhao, X.-J. In situ synthesis of molybdenum carbide/n-doped carbon hybrids as an efficient hydrogen-evolution electrocatalyst. *RSC Adv.* **2018**, *8*, 17202–17208. [CrossRef]

43. Chen, R.; Zhao, T.; Wu, W.; Wu, F.; Li, L.; Qian, J.; Xu, R.; Wu, H.; Albishri, H.M.; Al-Bogami, A. Free-standing hierarchically sandwich-type tungsten disulfide nanotubes/graphene anode for lithium-ion batteries. *Nano Lett.* **2014**, *14*, 5899–5904. [CrossRef] [PubMed]

44. Vikraman, D.; Hussain, S.; Truong, L.; Karuppasamy, K.; Kim, H.-J.; Maiyalagan, T.; Chun, S.-H.; Jung, J.; Kim, H.-S. Fabrication of MoS$_2$/WSe$_2$ heterostructures as electrocatalyst for enhanced hydrogen evolution reaction. *Appl. Surf. Sci.* **2019**, *480*, 611–620. [CrossRef]

45. Fan, X.; Zhou, H.; Guo, X. Wc nanocrystals grown on vertically aligned carbon nanotubes: An efficient and stable electrocatalyst for hydrogen evolution reaction. *ACS Nano* **2015**, *9*, 5125–5134. [CrossRef]

46. Xu, K.; Wang, F.; Wang, Z.; Zhan, X.; Wang, Q.; Cheng, Z.; Safdar, M.; He, J. Component-controllable WS$_{2(1-x)}$Se$_{2x}$ nanotubes for efficient hydrogen evolution reaction. *ACS Nano* **2014**, *8*, 8468–8476. [CrossRef]

47. Ma, L.; Ting, L.R.L.; Molinari, V.; Giordano, C.; Yeo, B.S. Efficient hydrogen evolution reaction catalyzed by molybdenum carbide and molybdenum nitride nanocatalysts synthesized via the urea glass route. *J. Mater. Chem. A* **2015**, *3*, 8361–8368. [CrossRef]

48. Zhang, K.; Zhao, Y.; Fu, D.; Chen, Y. Molybdenum carbide nanocrystal embedded n-doped carbon nanotubes as electrocatalysts for hydrogen generation. *J. Mater. Chem. A* **2015**, *3*, 5783–5788. [CrossRef]

49. Vikraman, D.; Hussain, S.; Akbar, K.; Truong, L.; Kathalingam, A.; Chun, S.-H.; Jung, J.; Park, H.J.; Kim, H.-S. Improved hydrogen evolution reaction performance using MoS$_2$–WS$_2$ heterostructures by physicochemical process. *ACS Sustain. Chem. Eng.* **2018**, *6*, 8400–8409. [CrossRef]

50. Li, Y.; Wang, H.; Xie, L.; Liang, Y.; Hong, G.; Dai, H. MoS$_2$ nanoparticles grown on graphene: An advanced catalyst for the hydrogen evolution reaction. *J. Am. Chem. Soc.* **2011**, *133*, 7296–7299. [CrossRef]

51. Zhang, K.; Li, C.; Zhao, Y.; Yu, X.; Chen, Y. Porous one-dimensional Mo$_2$C–amorphous carbon composites: High-efficient and durable electrocatalysts for hydrogen generation. *Phys. Chem. Chem. Phys.* **2015**, *17*, 16609–16614. [CrossRef] [PubMed]

52. Šljukić, B.; Vujković, M.; Amaral, L.; Santos, D.; Rocha, R.; Sequeira, C.; Figueiredo, J.L. Carbon-supported Mo$_2$C electrocatalysts for hydrogen evolution reaction. *J. Mater. Chem. A* **2015**, *3*, 15505–15512. [CrossRef]

53. Soon, J.M.; Loh, K.P. Electrochemical double-layer capacitance of MoS$_2$ nanowall films. *Electrochem. Solid State Lett.* **2007**, *10*, A250–A254. [CrossRef]

54. Chen, W.; Yu, X.; Zhao, Z.; Ji, S.; Feng, L. Hierarchical architecture of coupling graphene and 2D WS$_2$ for high-performance supercapacitor. *Electrochim. Acta* **2019**, *298*, 313–320. [CrossRef]

55. Zhai, Y.; Dou, Y.; Zhao, D.; Fulvio, P.F.; Mayes, R.T.; Dai, S. Carbon materials for chemical capacitive energy storage. *Adv. Mater.* **2011**, *23*, 4828–4850. [CrossRef] [PubMed]

56. Zhang, Y.; Ju, P.; Zhao, C.; Qian, X. In-situ grown of MoS$_2$/rGO/ MoS$_2$@Mo nanocomposite and its supercapacitor performance. *Electrochim. Acta* **2016**, *219*, 693–700. [CrossRef]

57. Huang, K.-J.; Wang, L.; Zhang, J.-Z.; Wang, L.-L.; Mo, Y.-P. One-step preparation of layered molybdenum disulfide/multi-walled carbon nanotube composites for enhanced performance supercapacitor. *Energy* **2014**, *67*, 234–240. [CrossRef]

58. Cao, Z.; Liu, C.; Huang, Y.; Gao, Y.; Wang, Y.; Li, Z.; Yan, Y.; Zhang, M. Oxygen-vacancy-rich NiCo$_2$O$_4$ nanoneedles electrode with poor crystallinity for high energy density all-solid-state symmetric supercapacitors. *J. Power Sources* **2020**, *449*, 227571. [CrossRef]

59. Balasingam, S.K.; Lee, M.; Kim, B.H.; Lee, J.S.; Jun, Y. Freeze-dried MoS$_2$ sponge electrodes for enhanced electrochemical energy storage. *Dalton Trans.* **2017**, *46*, 2122–2128. [CrossRef]

60. Pazhamalai, P.; Krishnamoorthy, K.; Manoharan, S.; Kim, S.-J. High energy symmetric supercapacitor based on mechanically delaminated few-layered MoS$_2$ sheets in organic electrolyte. *J. Alloys Compd.* **2019**, *771*, 803–809. [CrossRef]

61. Navarro-Suárez, A.M.; Van Aken, K.L.; Mathis, T.; Makaryan, T.; Yan, J.; Carretero-González, J.; Rojo, T.; Gogotsi, Y. Development of asymmetric supercapacitors with titanium carbide-reduced graphene oxide couples as electrodes. *Electrochim. Acta* **2018**, *259*, 752–761. [CrossRef]

62. Khawula, T.N.; Raju, K.; Franklyn, P.J.; Sigalas, I.; Ozoemena, K.I. Symmetric pseudocapacitors based on molybdenum disulfide (MoS_2)-modified carbon nanospheres: Correlating physicochemistry and synergistic interaction on energy storage. *J. Mater. Chem. A* **2016**, *4*, 6411–6425. [CrossRef]

63. Singh, K.; Kumar, S.; Agarwal, K.; Soni, K.; Gedela, V.R.; Ghosh, K. Three-dimensional graphene with MoS_2 nanohybrid as potential energy storage/transfer device. *Sci. Rep.* **2017**, *7*, 1–12.